Flagellar dynamics reveal fluctuations and kinetic limit in the *Escherichia coli* chemotaxis network

Roshni Bano[1,3], Patrick Mears[2,3], Ido Golding[1,2,3], Yann R. Chemla[1,2,3,*]

[1]*Center for Biophysics and Quantitative Biology, University of Illinois, Urbana-Champaign*

[2]*Department of Physics, University of Illinois, Urbana-Champaign*

[3]*Center for the Physics of Living Cells, University of Illinois, Urbana-Champaign*

*For correspondence: ychemla@illinois.edu

Abstract

The *Escherichia coli* chemotaxis network, by which bacteria modulate their random run/tumble swimming pattern to navigate their environment, must cope with unavoidable number fluctuations ("noise") in its molecular constituents like other signaling networks. The probability of clockwise (CW) flagellar rotation, or CW bias, is a measure of the chemotaxis network's output, and its temporal fluctuations provide a proxy for network noise. Here we quantify fluctuations in the chemotaxis signaling network from the switching statistics of flagella, observed using time-resolved fluorescence microscopy of individual optically trapped *E. coli* cells. This approach allows noise to be quantified across the dynamic range of the network. Large CW bias fluctuations are revealed at steady state, which may play a critical role in driving flagellar switching and cell tumbling. When the network is stimulated chemically to higher activity, fluctuations dramatically decrease. A stochastic theoretical model, inspired by work on gene expression noise, points to CheY activation occurring in bursts, driving CW bias fluctuations. This model also shows that an intrinsic kinetic ceiling on network activity places an upper limit on activated CheY and CW bias, which when encountered suppresses network fluctuations. This limit may also prevent cells from tumbling unproductively in steep gradients.

Introduction

A common feature of living organisms is their ability to sense environmental signals and respond to these signals by modifying their behavior. This ability is enabled by signal transduction, which converts environmental inputs into behavioral outputs[1]. Studies have shown that signaling networks must operate in the presence of noise not only in their inputs but also in the circuit components themselves[2,3]. Until recently, it was thought that signaling networks had evolved to be robust against undesirable noise[4–7]. More recent studies have shifted to understanding the role of noise in regulating and fine-tuning biological function[8,9]. For example, noise resulting from transcription/translation has been measured precisely and shown to play a critical role in networks for gene expression and regulation[10–12]. In contrast, studying noise resulting from signaling networks at the post-translation level has proven more challenging.

One extensively studied signaling system is the chemotaxis network of *E. coli*, which cells use to navigate their environment[13–17]. *E. coli* cells swim in a random walk consisting of "runs"—during which their flagella rotate counter-clockwise (CCW)—and "tumbles"—during which one or more flagella rotate clockwise (CW)[18–21]. Changing environmental conditions are sensed through a two-component signaling system comprising receptors that bind extracellular ligands and a kinase, CheA, that transfers its phosphoryl group onto downstream effectors[22]. The response regulator, CheY, when phosphorylated by the receptor kinase complex to CheY-P, binds to the flagellar motor and increases the probability of CW motor rotation[23–25]. The phosphatase CheZ carries out the opposite reaction, maintaining a dynamic equilibrium between CheY and CheY-P (**Figure 1a**)[26,27]. Additionally, the methyltransferase CheR and the methylesterase CheB covalently modify receptors, and the resulting modulation of CheA activity affects CheY-P levels over the timescales of chemotactic adaptation[28–30]. While the population-averaged relationships between these signaling protein concentrations and cellular motility in *E. coli* are now well understood[13–16,24], the role of fluctuations in modulating cell behavior remains comparatively unexplored.

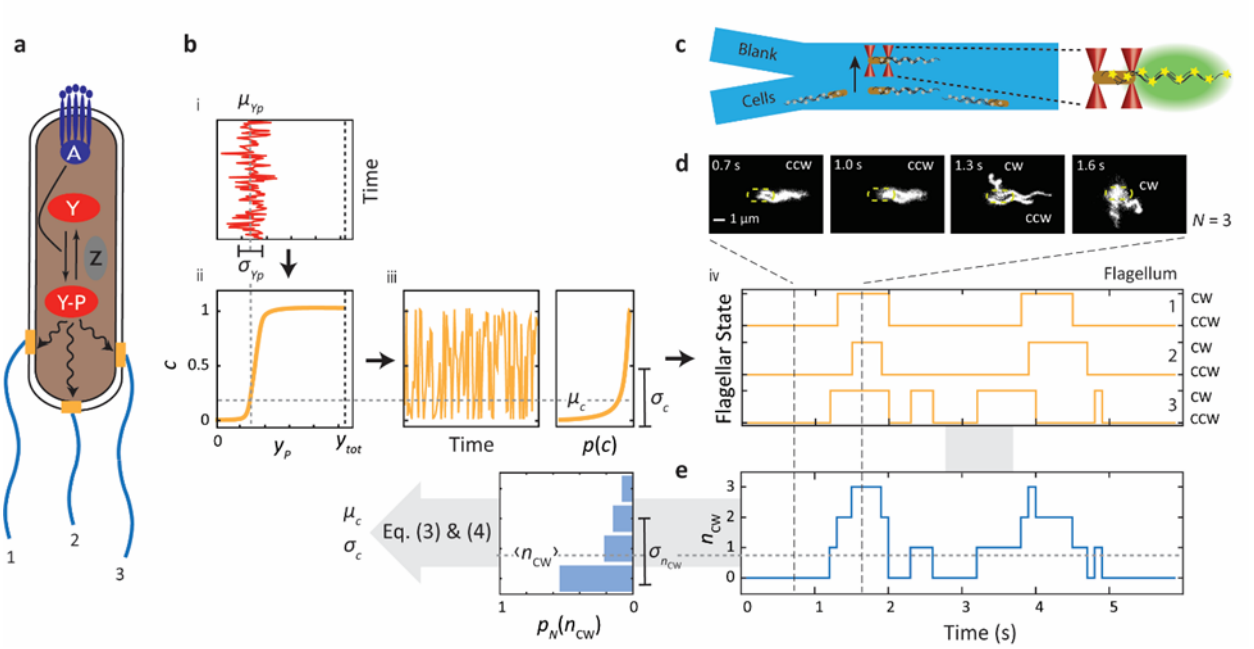

Figure 1. Estimating the temporal motor bias fluctuations from flagellar dynamics of single *E. coli* cells. a. Schematic of a multi-flagellated *E. coli* cell showing key reactions of the chemotaxis signaling network. CheY is phosphorylated to CheY-P by the receptor kinase complex (CheA; dark blue); CheY-P is dephosphorylated by the phosphatase CheZ (gray). CheY-P binding to flagellar motors (mustard) causes a switch from CCW to CW rotation, which leads to cell tumbling. **b.** Temporal fluctuations in [CheY-P] due to chemotaxis network dynamics and their effect on flagellar switching statistics. (i) [CheY-P] temporal fluctuations. (ii) Switch-like response of motor CW bias, c, to [CheY-P]. (iii) Resulting temporal fluctuations in motor bias $c(t)$ and its distribution $p(c)$, characterized by the mean μ_c and standard deviation σ_c. (iv) CCW/CW rotation state of three independent flagellar motors corresponding to the instantaneous motor bias c. **c.** Schematic of two-channel laminar flow chamber for optical trap assay. A single cell with fluorescently labelled flagella (gray stars) is captured from the bottom channel ("Cells"), aligned along the flow between two optical traps (red cones), moved to the upper channel ("Blank"), and its fluorescent flagella (yellow stars) imaged by stroboscopic slim-field microscopy (green). **d.** Fluorescence data trace from representative trapped cell with $N = 3$ flagella. Top, still images of fluorescent flagella, with position of the unlabeled cell body approximately indicated by the dashed yellow line. CW and CCW rotating flagella are labelled where clearly visible. Middle, CCW/CW rotation state of each flagellum vs. time (mustard). Bottom, corresponding number n_{CW} of CW flagella vs. time (light blue). **e**. Probability distribution $p_N(n_{CW})$, determined experimentally from d (light blue bars). The mean μ_c and standard deviation σ_c of the motor bias are estimated from the parameters of the distribution $p_N(n_{CW})$ using Eqs. (3) and (4).

Noise in the chemotaxis network was first inferred by Korobkova et al.[31] from long-term measurements of individual rotating flagellar motors. Inside the cell, the CheY-P concentration

[CheY-P] fluctuates in time due to noise sources upstream in the signaling network (**Figure 1b, i**). These fluctuations in turn affect downstream behavior. The motor CW bias, i.e. the probability of CW rotation of a single flagellar motor, has an ultrasensitive switch-like dependence[25] on the intracellular [CheY-P] (**Figure 1b, ii**), resulting in fluctuations in motor rotational state (**Figure 1b, iii**) and in the cell's swimming behavior. Noise in the *E. coli* chemotaxis signaling network is thought to have functional consequences for sensing and navigation in complex natural microenvironments. It has been proposed to allow cells to sample 3-D space more effectively[31,32], enhance chemotactic drift up a gradient[33–35], and synchronize flagellar switching to mitigate differences in swimming behavior among cells with different numbers of flagella[36,37].

Here, we use optical trapping coupled with time-resolved fluorescence microscopy[37,38] to infer temporal network fluctuations from the statistics of flagellar switching in individual multi-flagellated *E. coli* cells. Analyzing cells at steady state, we determine the mean and fluctuations in CW bias, which reveal that the network is poised at a low CW bias, favoring CCW flagellar rotation/running, and that transient fluctuations drive CW flagellar rotation/tumbling. Previous studies using flagellar motor behavior[31,39] or fluorescence-based reporters[40,41] to infer noise in the chemotaxis network have been limited to long timescales (>10 s) due to temporal averaging. However, studies of flagellar tracking show that short timescale fluctuations are important to explain observations of correlated flagellar switching[36,42]. In contrast to most earlier approaches, our method measures fluctuations on shorter timescales (~3 s), comparable to individual run and tumble durations. We exploit this feature to track carefully the time evolution of signaling noise in cells responding to a stimulus that increases CheA activity. This, in turn, allows us to measure network fluctuations across the accessible range of motor CW biases. We find that fluctuations are significantly reduced when the motor CW bias is increased away from its steady-state value. A simple stochastic model in which noise in signaling arises from burst-like fluctuations in CheA activity recapitulates all of our experimental results and suggests that the decrease in fluctuations upon stimulation is due to a kinetic ceiling on the CheA activity.

Results

Flagellar switching statistics reveal temporal network fluctuations

We inferred the temporal fluctuations in the chemotaxis network from the dynamics of flagellar switching in individual cells. We imaged fluorescently labeled flagella on individual, swimming cells to determine their CCW/CW rotation state, using an optical trapping assay described previously[37,38,43] (see **Materials and Methods**). Briefly, *E. coli* cells were injected into a laminar flow chamber containing two parallel channels. A single cell was captured using a dual beam optical trap from one channel containing many cells (labeled "cells" in **Figure 1c**) and moved for observation to a second channel containing no other cells (labeled "blank" in **Figure 1c**). The light scattered by the optically trapped cell was used to monitor the run/tumble swimming behavior as described previously (data not shown, see Ref. [38]). Simultaneously, high-speed, epi-fluorescent stroboscopic imaging[37] was used to monitor the rotation state of all the individual flagella on the cell at high temporal resolution (0.1 s) and long-time duration (ranging from ~15 to 40 s, until the flagella photobleached) (**Figure 1d,** top). Following Darnton et al.[21] and our previous work[39], the CCW/CW rotation state of each flagellum was visually identified by its different helical waveforms (see **Materials and Methods**).

We next inferred network fluctuations making use of the statistics of switching in multi-flagellated cells. For a cell with N flagellar motors, the probability that n_{cw} rotate in a CW direction, $p_N(n_{cw})$, is equal to (see **Materials and Methods**):

$$p_N(n_{cw}) = \int_0^1 dc\, p_N(n_{cw} \mid c) p(c), \tag{1}$$

where c is the instantaneous motor CW bias, or probability that a motor rotates CW, $p_N(n_{cw} \mid c)$ is the conditional probability that n_{cw} out of N motors are in the CW state given a certain c, and $p(c)$ is the distribution of CW biases (**Figure 1b, iii**). Previous work in which flagellar motor switching was decoupled from the chemotaxis signaling network shows that the motors independently sense the intracellular CheY-P concentration[37]. Thus, $p_N(n_{cw} \mid c)$, represents the conditional probability of the collective CW state of the flagella motors and is given by the binomial distribution:

$$p_N(n_{cw} \mid c) = \binom{N}{n_{cw}} c^{n_{cw}} (1-c)^{N-n_{cw}}. \tag{2}$$

129 Since the conditional probability is known, Eq. (1) in principle allows one to connect the
130 probability $p_N(n_{cw})$—which can be determined from measurements of the CCW/CW rotational
131 state of each flagellum of a cell with *N* flagellar motors—to the distribution of CW biases *p*(*c*). In
132 practice, a solution to Eq. (1) is not unique, but an increasing number of moments of *p*(*c*) can be
133 determined as the number of flagella *N* increases. Specifically, from Eqs. (1) and (2), the mean
134 and variance in the number of CW flagella n_{cw} can be shown to be (see **Materials and Methods**)

135 $$\langle n_{cw} \rangle = N\mu_c, \tag{3}$$

136 and

137 $$\sigma_{n_{cw}}^2 = \langle n_{cw}^2 \rangle - \langle n_{cw} \rangle^2 = N\mu_c(1-\mu_c) + N(N-1)\sigma_c^2, \tag{4}$$

138 where μ_c and σ_c are the mean and standard deviation in CW bias. In Eq. (4) the first term
139 represents the fluctuations in $p_N(n_{cw})$ intrinsic to switching of *N* independent flagellar motors;
140 the second term represents the additional contribution from fluctuations in CW bias. These
141 expressions show that by analyzing cells with $N \geq 2$ flagella, one can determine the mean and
142 fluctuations in CW bias over a given time window.

143 **Figure 1** shows the workflow to determine network fluctuations experimentally.
144 Fluorescence tracking of the CCW/CW state of the individual flagella (**Figure 1d,** middle) is
145 represented as a time trace of the number of CW flagella (**Figure 1d,** bottom). For a cell with *N*
146 flagella, a histogram of this time trace was used to construct the probability distribution $p_N(n_{cw})$
147 that n_{cw} out of *N* flagella rotate CW (**Figure 1e**), from which the mean and standard deviation in
148 n_{cw} were calculated. Using Eqs. (3) and (4) the mean, μ_c, and standard deviation, σ_c, in CW bias
149 for the cell were determined (**Figure 1e**).

150

151 **Cells at steady state exhibit large CW bias fluctuations**

152 We first applied the above approach to free-swimming (i.e. unstimulated) cells for which the
153 chemotaxis network is in a steady state. Fluorescence tracking data of CCW/CW flagellar states
154 were obtained for cells of a strain wild-type for chemotaxis (HCB1660, henceforth referred to as
155 "wild-type"; see **Materials and Methods**) with *N* = 2 to 5 flagella. Data traces tracking n_{cw} were

pooled together from multiple cells with the same total number of flagella N to generate $p_N(n_{cw})$ (**Figure 2a**, colored histograms; number of cells = 13, 15, 14, 9 for N = 2, 3, 4, 5 flagella, respectively). As we show below, pooling over the population of cells did not affect our results appreciably.

Figures 2b-c shows the mean, μ_c, and coefficient of variation (CV), σ_c/μ_c in CW bias for each set of cells with different number of flagella N, as determined from Eqs. (3) and (4). Errors in μ_c and σ_c/μ_c were estimated by bootstrapping over the population of cells with the same N (see **Materials and Methods**). The parameter values did not appear to depend strongly on N, consistent with our expectation that the number of flagella should not affect network fluctuations measurably. Thus, we also analyzed the data globally, carrying out a weighted average over all cells (number of cells = 51) to determine $\langle\mu_c\rangle = 0.12 \pm 0.01$ and $\langle\sigma_c/\mu_c\rangle = 1.5 \pm 0.2$ (see **Materials and Methods**). A CV > 1 shows that the chemotaxis network in free-swimming wild-type cells exhibits a high degree of fluctuations.

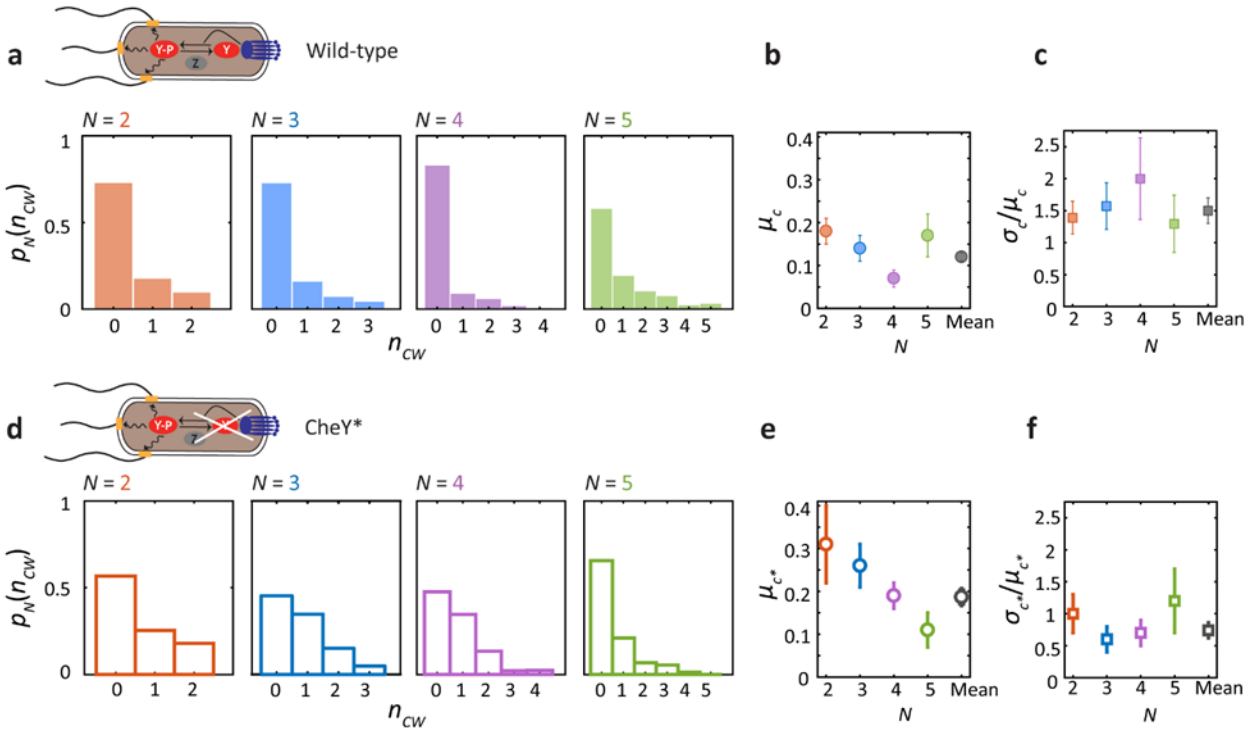

Figure 2. Motor bias fluctuations in the chemotaxis network at steady state. Measurement of flagellar dynamics and estimation of motor bias fluctuations in wild-type *E. coli* strain HCB1660 (a-c) and in "CheY*" mutant strain PM87 expressing constitutively active CheY^{D13K} (d-f). **a.** Experimentally determined probability distribution $p_N(n_{CW})$ that n_{CW}

173 out of N flagella rotate CW, grouped by cells with the same total number of flagella N = 2, 3, 4, 5 (number of cells =
174 13, 15, 14, 9 respectively). **b.** Mean motor bias, μ_c, determined separately for each N (colored filled circles) and the
175 mean across N (gray filled circle). **c.** Coefficient of variation in motor bias, σ_c/μ_c, determined separately for each N
176 (colored filled squares) and the mean across N (gray filled squares) **d-f.** Same as a-c for CheY* strain, showing
177 experimental distributions (open bars) and estimated motor bias parameters (open circles and squares), grouped by
178 cells with the same total number of flagella N = 2, 3, 4, 5 (number of cells = 13, 13, 9, 9 respectively).
179

180 We carried out several tests to confirm that the observed fluctuations in CW bias resulted
181 from noise in signal transduction. First, we applied our method of analysis to a strain that
182 expresses the constitutively active mutant protein $CheY^{D13K}$, a mimic for CheY-P[24] (strain PM87,
183 henceforth referred to as "CheY*"; see **Materials and Methods**). Since CheY in this strain is
184 decoupled from the upstream network components and the concentration of $CheY^{D13K}$ is
185 determined from gene expression levels, which should not fluctuate on the timescales of our
186 experiments in nutrient-limited conditions[44], we expected to observe smaller fluctuations in CW
187 bias as compared to the wild-type strain. Repeating the above analysis, **Figure 2d** show the
188 experimental distributions $p_N(n_{cw})$. Values for the mean, standard deviation, and CV in CW bias
189 are found in **Tables 3** and **4**. Comparing **Figs. 2b-c** and **2e-f**, the mean CW bias is similar for both
190 strains (0.12 ± 0.01 and 0.19 ± 0.02, respectively), and, as expected, fluctuations in the CheY*
191 strain (number of cells = 13, 13, 9, 9 for N = 2, 3, 4, 5 flagella, respectively) are reduced compared
192 to the wild-type strain, yielding $\langle\sigma_c/\mu_c\rangle$ = 0.7 ± 0.2 (total number of cells = 44).

193 Second, we tested whether the variance in CW bias could be due to cell-to-cell differences in
194 mean CW bias rather than fluctuations arising in signal transduction. To test the contribution of
195 cell-to-cell variation, we carried out the above analysis over individual cell traces and compared
196 the wild-type and CheY* strains. As shown in **Figure 3a** and **3b**, while the mean CW bias, μ_c, from
197 individual cell distributions was similar for both strains, the CV, σ_c/μ_c, was significantly smaller for
198 the CheY* strain as compared to the wild-type strain ($p \leq 0.05$; determined using a Wilcoxon rank
199 sum test), as expected. Errors in μ_c and σ_c/μ_c for individual cells were again determined by
200 bootstrapping (see **Materials and Methods**). Importantly, the coefficient of variation for
201 individual wild-type cells averaged over all cells with different N, $\langle\sigma_c/\mu_c\rangle \approx 1.5$, was close to that
202 determined over the population. This indicates that cell-to-cell variation over the wild-type cell

203 population does not contribute greatly to the variance in CW bias. In contrast, the CV was
204 significantly smaller for individual cells of the CheY* strain; $\langle\sigma_c/\mu_c\rangle \approx 0.4$, as compared to 0.7 over
205 the population. We suspect cell-to-cell CheY^{D13K} expression differences may contribute to the
206 estimated fluctuations in **Figures 2e-f**. Furthermore, we carried out a variance decomposition
207 analysis to identify the contribution of cell-to-cell differences to the variance in CW bias
208 measured over the cell population (see **Materials and Methods**). Consistent with the results
209 above, we found that only 20% of the variance in CW bias for wild-type cells resulted from cell-
210 to-cell differences, compared to 70% for CheY* cells. Our results thus show that we can attribute
211 the observed variance in CW bias for wild-type cells to fluctuations due to signaling activity in
212 individual cells.

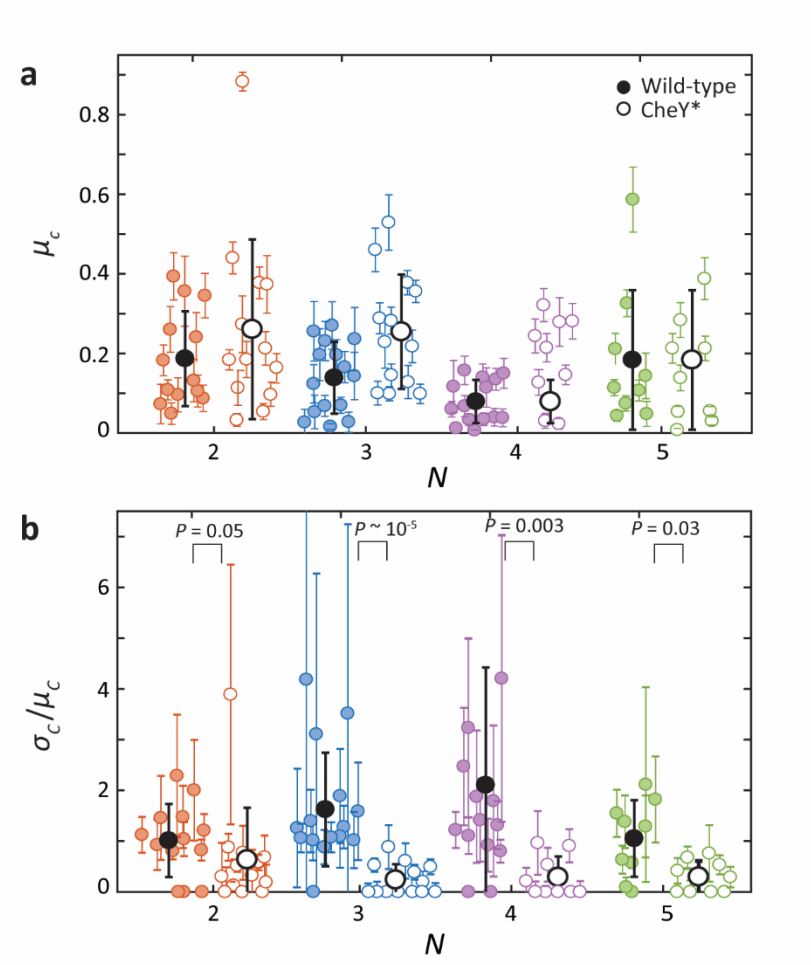

213

214 **Figure 3. Estimate of the mean and coefficient of variation of motor bias in individual cells. A.** Comparison of mean
215 motor bias, μ_c, determined for individual wild-type (colored circles) and CheY* cells (open circles), for different
216 number of flagella N. **b.** Comparison of the coefficient of variation in motor bias, σ_c/μ_c, determined for individual

217 wild-type (colored circles) and CheY* cells (open circles), for different *N*. Averages over each cell population are
218 overlaid (black solid circles for wild-type, black open circles for CheY*); error bars represent standard deviation. P-
219 values were determined using a Wilcoxon rank sum test.
220
221 Our method for determining network fluctuations allows us to make an important
222 observation: the mean CW bias in free swimming cells is low (0.12), while the fluctuations in CW
223 bias are very large (CV of 1.5). Thus the picture emerges of a network poised at low CW bias,
224 corresponding to CCW flagellar rotation and running, with large fluctuations driving CW flagellar
225 rotation and tumbling. This picture is consistent with simulations from Dufour et al.[45] as well as
226 experiments from Wong-Ng et al.[46] showing that cells' migration speed along chemical gradients
227 is maximized at very low CW bias[47]. All these observations suggest that the network operates at
228 a point to optimize chemotactic drift, and that fluctuations function to expand the allowed range
229 of run/tumble behavior of the cell.
230
231 **Fluctuations decrease upon stimulating the network to increase CW bias**
232 Having characterized fluctuations in the chemotactic network in the steady state, we next
233 investigated them in a network stimulated by a perturbation. In response to a stepwise change
234 in chemical environment, the intracellular [CheY-P] changes rapidly, and then reverts to its
235 steady-state value through adaptation[48–50]. Applying a large stepwise decrease in attractant leads
236 to a transient increase in [CheY-P] and in motor CW bias, followed by a decrease to the steady
237 state[43,51], allowing us to measure network fluctuations across the accessible range of motor CW
238 biases.
239 We measured the response of individual cells to a decrease in concentration of α-methyl-DL-
240 aspartate (MeAsp), a non-metabolizable analog of L-aspartate[52] that acts as a
241 chemoattractant[52,53]. We used a three-channel flow chamber (**Figure 4a**) to observe the effect of
242 a step-down from 1 to 0 mM MeAsp on individual optically trapped wild-type cells. The step-
243 down was applied by quickly moving a trapped cell from the middle channel of the flow chamber
244 containing 1 mM MeAsp (**Figure 4a**; labeled "blank + attractant") to the top channel containing
245 no MeAsp (labeled "blank"; see **Materials and Methods**). The run-tumble behavior of the cell

246 was monitored pre- and post-stimulus via the optical traps (see **Materials and Methods**),
247 whereas the flagellar rotation state was measured by fluorescence imaging only post-stimulus.
248 **Figure 4b** shows a representative measurement of a cell with 3 flagella undergoing a step-
249 down stimulus, where we define $t = 0$ as the time at which the trapped cell has finished moving
250 to the channel with no MeAsp. In response, the cell exhibits the expected increase in tumbling
251 immediately post-stimulus, followed by relaxation to the pre-stimulus steady state as the cell
252 adapts (**Supplementary Figure S1**). As the probability of tumbling is directly related to the
253 probability of CW flagellar rotation[37], n_{cw} measured by fluorescence imaging post-stimulus also
254 relaxes to lower values as the cell adapts (**Figure 4b**, blue trace). Since the motor bias is time-
255 dependent in cells responding to a step-down, the time traces of n_{cw} for each cell were divided
256 into time windows corresponding to 20% of the cell's adaptation time, or ~2.6 s on average
257 (**Figure 4c**, colors corresponding to time window), over which the average tumble bias was
258 constant to within ~10-20% (see **Materials and Methods** for more details on windowing). All data
259 from cells with the same total number of flagella (in **Figure 4c**, three representative cells with N
260 = 3 flagella) were pooled in similarly constructed time windows and used to create histograms
261 $p_N(n_{cw})$ at each time (**Figure 4d**). The mean and CV in the CW bias were then estimated separately
262 for each window (**Figure 4e-f**, colored data points). Relative to unstimulated cells (**Figure 4e**, gray
263 data points for unstimulated wild-type cells with N = 3 flagella), the mean CW bias shifted to a
264 higher value immediately after the stimulus, as expected for a step down. Interestingly, the CV
265 in CW bias decreased (**Figure 4f**). We verified that the reduction in noise was due to a change in
266 chemotaxis network dynamics after stimulation rather than due to windowing of the data; the
267 standard deviations in CW bias in adapting cells were significantly different compared to those in
268 steady-state cells over similarly sized 3-s time windows ($p \leq 0.05$).
269 The time-dependent, post-stimulus mean CW bias μ_c and coefficient of variation σ_c/μ_c for
270 cells with N = 2, 3, 4 flagella are shown in **Figure 5a** and **5b** (colored filled circles; number of cells
271 = 8, 9, 9), respectively. The corresponding steady-state mean and coefficient of variation
272 obtained from **Figure 2** are also plotted for reference (for $t < 0$, colored open circles). As
273 expected, the trends are similar for cells with different numbers of flagella. Thus, we also show
274 these parameters determined globally for each time window by a weighted average across cells

with different *N* (**Figure 5a** and **5b**; gray filled circles; see **Materials and Methods**). Consistent with **Figure 4e-f**, the mean CW bias increases immediately in response to the step-down stimulus and relaxes toward its steady-state, pre-stimulus value as the cells adapt, whereas the CV in CW bias falls post-stimulus, then gradually increases toward the pre-stimulus value.

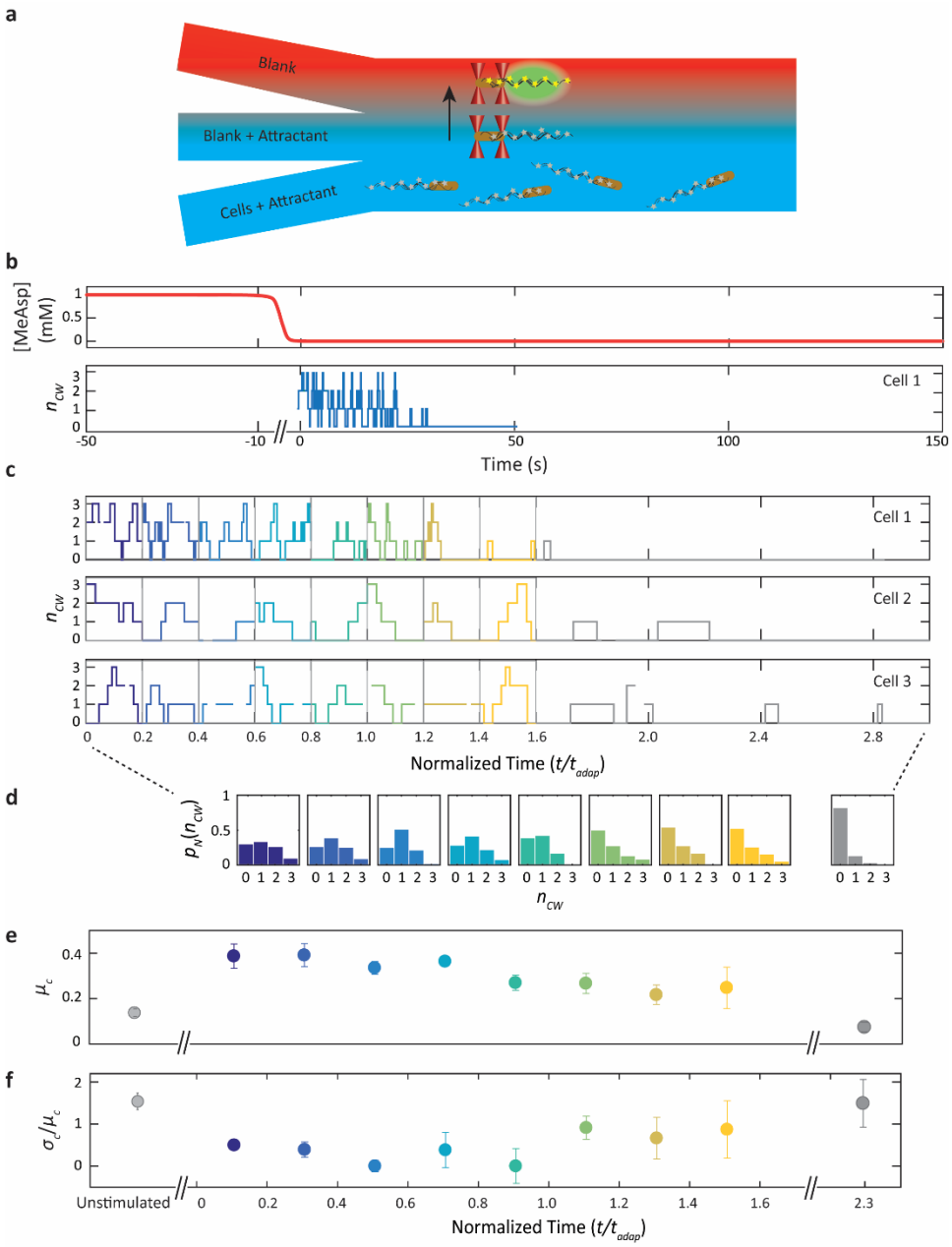

Figure 4. Motor bias fluctuations in the chemotaxis network upon stimulation. a. Schematic of three-channel laminar flow chamber for flagellar imaging of a cell experiencing a step down in attractant concentration. A single

cell with fluorescently labelled flagella (gray stars) is captured from the bottom channel containing 1 mM MeAsp ("Cells + Attractant") and aligned along the flow between two optical traps (red cones) in the middle channel ("Blank + attractant"). The trapped cell is then moved to the upper channel lacking MeAsp ("Blank") and its fluorescent flagella (yellow stars) are imaged (green). **b.** Representative trace showing the response of "Cell 1" to a step-down stimulus. Top, schematic of MeAsp concentration over time, showing the step down from 1 to 0 mM. Data are not collected during the move from the middle to the top channel. Bottom, number n_{CW} of CW flagella over time after the move has finished at $t = 0$. **c-e.** Estimation of motor bias fluctuations in cells responding to a step-down stimulus. **c.** Traces from three representative "Cells 1, 2, 3" showing the number n_{CW} of CW flagella vs. time (normalized by each cell's adaptation time t_{adap}). Each trace is subdivided into windows of duration $0.2t_{adap}$, and data from each window is pooled across cells (for $N = 3$ flagella shown here, number of cells = 9). **d.** Distributions of the number of CW flagella $p_N(n_{CW})$ for each window (colored bars) **e**. Mean motor bias μ_c corresponding to each window and for unstimulated cells (gray) as comparison. **f**. Coefficient of variation in motor bias σ_c/μ_c corresponding to each window, and for unstimulated cells.

These results point to two interesting features. First, the mean CW bias shows an almost 300% increase compared to the pre-stimulus steady state immediately after the step down (**Figure 5a**). While the increase in CW bias is expected for a step-down stimulus, it is smaller in magnitude than predicted by existing models[54,55]. Given the strength of the stimulus (from 1 to 0 mM [MeAsp]), these models predict a CW bias close to 1; instead, the CW bias remains near 0.5. Second, fluctuations are significantly reduced immediately after the stimulus is applied, decreasing from $\sigma_c/\mu_c = 1.5$ pre-stimulus to as low as $\sigma_c/\mu_c = 0.25$ post-stimulus (**Figure 5b**). This value is lower than that measured in individual CheY* cells (**Figure 3b**), suggesting that fluctuations in the network are largely suppressed when driven to high CW bias. Noise suppression has previously been mentioned in the opposite limit[56] when the network is driven to low activity by a step-up stimulus.

To summarize all of the experimental data, we plotted in **Figure 5c** the coefficient of variation vs. the mean CW bias for cells at steady state (open circles) and for stimulated cells (filled circles). All of the data fall on one continuous curve, which shows how network fluctuations vary across the accessible range of motor CW bias. Across all data sets, fluctuations uniformly exhibit the same behavior: a decreasing trend from high variance ($\sigma_c/\mu_c > 1$) at low CW bias, approaching zero at a CW bias of 0.5. For many biological networks, the relationship between the CV (or

variance) and mean has proven useful in understanding the noise characteristics of the network[9,57]. For instance, Poisson-distributed noise is manifested by a CV decreasing as 1/mean$^{0.5}$. Here, the trend can be fit to a line of form $C_0(1-\mu_c/\mu_{c,\max})$, with C_0 = 1.4 and $\mu_{c,\max}$ ≈ 0.5, (solid line, **Figure 5c**). In the following discussion, we propose a model to interpret this trend and to understand the network noise characteristics they represent.

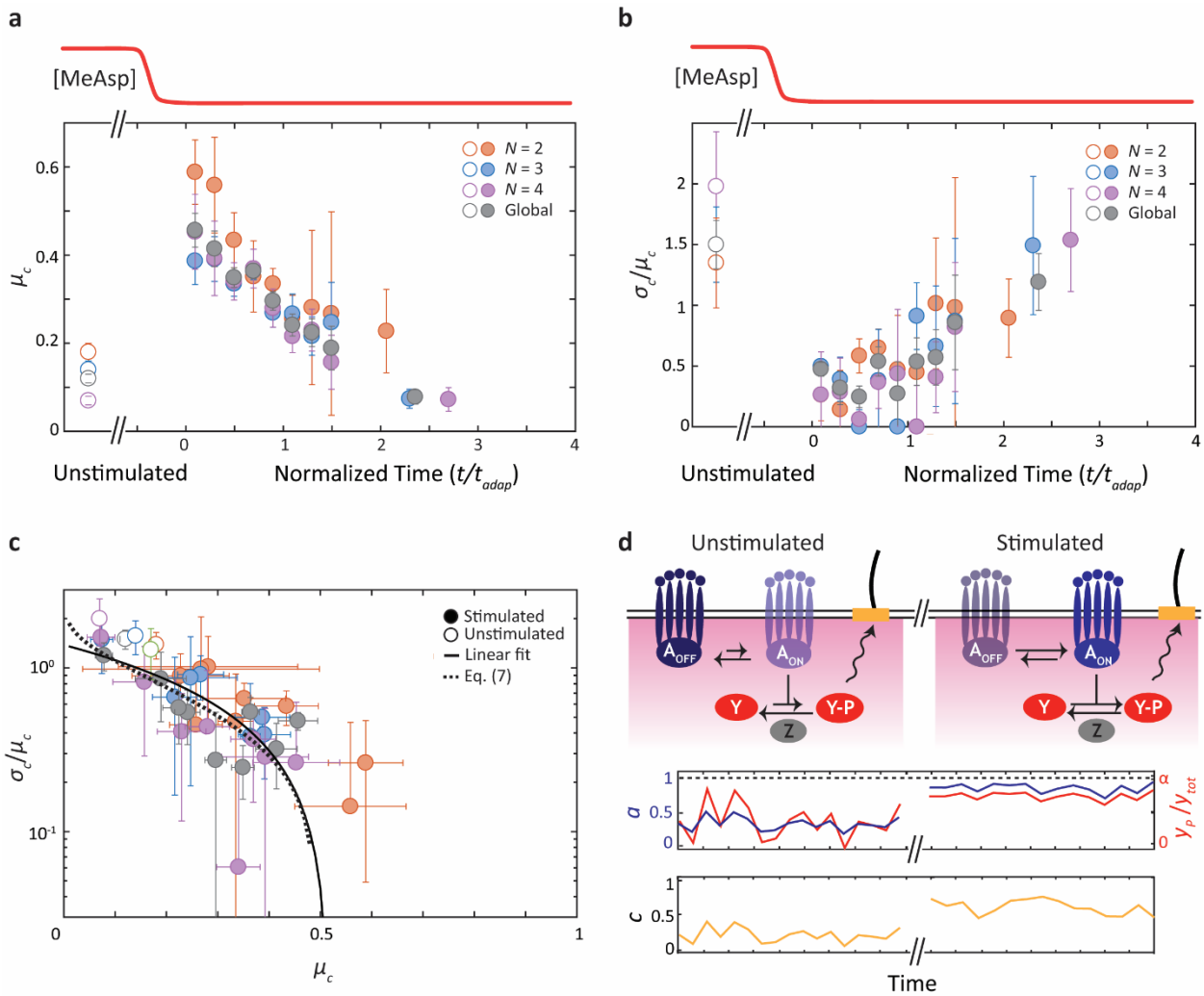

Figure 5. Reduction in motor bias fluctuations post stimulus due to kinase phosphorylation dynamics. a. Mean motor bias, μ_c, vs. normalized time t/t_{adap} after step down stimulus (top schematic, red) determined separately for each number of flagella N (colored circles) and averaged across N (gray circles). **b.** Coefficient of variation in motor bias, σ_c/μ_c, after step down. Same color code as a. Data are pooled by cells with the same total number of flagella N = 2, 3, 4 (number of cells = 8, 9, 9). The pre-stimulus mean and coefficient of variation in motor bias were obtained from the analysis of the unstimulated cells in Fig. 2. **c.** Coefficient of variation in motor bias, σ_c/μ_c,

plotted against the mean motor bias, μ_c, for data from unstimulated and stimulated cells from a and b**.** Fits to a line (solid line) and to a model of network noise (dotted line; see Eq. (7)) are also shown. **d.** Simple model of network fluctuations in *E. coli*. (Left) In unstimulated cells at steady state, fluctuations in CheA activity (dark blue) produce bursts of CheY-P production (red) and high motor bias fluctuations (mustard). (Right) In stimulated cells, CheA activity is increases and shows reduced fluctuations as it approaches the kinetic ceiling. This also causes a reduction in [CheY-P] fluctuations and in motor bias fluctuations at high mean [CheY-P].

Discussion

In this work we demonstrate a new approach for inferring fluctuations in the chemotaxis network based on the statistics of flagellar switching in multi-flagellated *E. coli* cells. One advantage of this approach is that its accuracy in quantifying network noise does not depend on temporal averaging, which limited previous measurements to long time scales (>10 s)[31,39–41]. Many recent measurements of network noise have been made through FRET imaging systems that require data collection and averaging over long periods of time, and thus sacrifice temporal resolution. Single flagellar tracking using high speed cameras has emerged as an alternative to measure network noise at short timescales[36], and only very recently has revealed short time fluctuations (<1s)[58]. Our approach to estimating network noise relies on fluorescence-based observations of multiple flagellar motors making independent simultaneous "measurements" of the intracellular CheY-P level, and tuning their CW bias in response. This feature makes it possible to measure fluctuations in CW bias (and infer the underlying network noise) over time scales of individual runs and tumbles and to track their time evolution. As demonstrated in **Figure 4**, we can accurately determine the CV in CW bias over a ~3-s time window (see **Materials and Methods**; this time resolution can in principle be improved further by pooling over a larger number of cells). In turn, studying cells as they undergo adaptation enables us to quantify network fluctuations across the accessible range of motor CW biases, as summarized in **Figure 5**.

In **Figure 5c** the relationship between the CV and mean in CW bias provides a signature for the underlying *E. coli* chemotaxis signaling network noise, against which we can test various models. We thus sought a quantitative model to reproduce the noise characteristics we observed. The CW bias of every flagellar motor depends on the CheY-P concentration in an

356 ultrasensitive switch-like manner (**Figure 1b, ii**)[25], customarily modeled by a sigmoidal Hill
357 equation of the form

358 $$c(y_P) = \frac{y_P^H}{y_P^H + K^H}, \quad (5)$$

359 where $y_P \equiv$ [CheY-P], K is the CheY-P concentration at 0.5 CW bias, and H is the Hill coefficient.
360 (For cells at steady state, $K \approx 3.1$ μM and H is expected to be ~20[59].) Due to this switch-like
361 dependence, c is sensitive to small temporal fluctuations in [CheY-P]. CheY undergoes fast
362 phosphorylation-dephosphorylation reactions (**Figure 1a**), which lead to number fluctuations in
363 CheY-P (**Figure 1b, i**):

364 $$\text{CheY} \underset{k_z}{\overset{k_A a}{\rightleftharpoons}} \text{CheY-P}. \quad (6)$$

365 Here, the rate of CheY phosphorylation by the CheA-receptor complex is written as $k_A a$, where a
366 is the probability that CheA is in its active state and k_A is the maximum phosphorylation rate[60,61],
367 and k_Z is the rate of CheY-P dephosphorylation by the phosphatase CheZ. The intracellular [CheY-
368 P] fluctuates due in part to the stochastic nature of the reactions in Eq. (6) and in part to
369 fluctuations in the CheA kinase activity a itself[31,41].

370 In **SI discussion**, we examine how different sources of noise can reproduce the observed
371 behavior in CW bias fluctuations. Simple models incorporating CheY-P number fluctuations
372 through Eq. (6) do not recapitulate the experimental trends. The main issue is that these models
373 predict that CW bias fluctuations should to tend to zero as c approaches 1. This behavior occurs
374 because $c(y_P)$, in Eq. (5), exhibits a plateau when [CheY-P] >> K, making it insensitive to
375 fluctuations in [CheY-P] when CW bias is close to unity. However, as our data in **Figure 5c** shows,
376 σ_c/μ_c decreases to zero when CW bias = 0.5. Lele et al.[62] previously carried out experiments ruling
377 out the possibility of a plateau in c vs [CheY-P] at intermediate CW bias levels. This finding
378 suggests that CheY-P fluctuations themselves must be suppressed when c = 0.5.

379 One possibility to account for this observation is that there exists a cap on the amount of
380 CheY available for phosphorylation. For example, if such a cap limited the maximum CheY-P
381 concentration to [CheY-P] ≈ K, then network fluctuations would be suppressed near a CW bias of
382 0.5 according to Eq. (5). To test this mechanism, we constructed a mutant *ΔcheZ* strain ("RB03";

see **Materials and Methods**) lacking the phosphatase CheZ, in which all the available CheY is expected to be phosphorylated. Replicating our flagellar imaging analysis for this strain resulted in a mean CW bias of 0.99 ± 0.01 (data not shown), higher than that observed following a step-down stimulus, ruling out such a mechanism. (The CV for this strain was 0.02; data not shown.) This result is consistent with estimates of the total concentration of CheY of ~10 μM >> K[55]. An alternative possibility is that there exists a kinetic ceiling on the CheA-receptor complex, which limits the amount of CheY that can be phosphorylated at any one time. Since CheY-P undergoes dephosphorylation in the reaction scheme Eq. (6), the fraction of CheY that is phosphorylated must be less than one even when CheA is maximally active. Such a ceiling in the maximum [CheY-P] would lead to a reduction in [CheY-P] fluctuations.

To explore the latter mechanism quantitatively, we considered a comprehensive model taking into account fluctuations in CheY-P number and in the activity of the CheA-receptor complex during phosphorylation-dephosphorylation kinetics. To model CheA fluctuations, we allowed CheA to interconvert between active and inactive states, leading to a fluctuating activity $a(t)$. Adapting the approach of Paulsson et al.[57,63] used to model gene expression noise, we derived an analytical solution for the coefficient of variation in [CheY-P] in the presence of CheA fluctuations (see **SI Discussion**). Writing this expression in terms of CW bias gives

$$\frac{\sigma_c}{\mu_c} = H(1-c)\sqrt{\frac{\tau_Y}{\tau_Y+\tau_c}\frac{1}{\mu_{y_P}V_C}\left(1-\frac{\mu_{y_P}}{y_{tot}}\right)\left[1+\langle b\rangle\left(1-\frac{\mu_{y_P}}{\alpha y_{tot}}\right)\right]}. \tag{7}$$

The appearance of the Hill coefficient H in Eq. (7) follows from the coupling of CheY-P fluctuations to those in CW bias c in Eq. (5). Here, τ_c is the characteristic timescale for motor switching and $\tau_Y = (k_A a + k_Z)^{-1}$ is that for CheY phosphorylation-dephosphorylation; the factor that depends on τ_c and τ_y accounts for temporal averaging that results from the different fluctuation timescales for motor switching and CheY reactions. The other factors inside the square root represent the number fluctuations in CheY-P; $y_{tot} \approx 10$ μM is the total CheY concentration inside the cell, and V_C is the *E. coli* cell volume, assumed to be 1.4 fL[64] ($V_C^{-1} \approx 1.2$ nM). The factor in brackets specifically represents the contribution from CheA activity fluctuations. Here $\langle b\rangle$ denotes the number of

409 new CheY-P generated during the time periods when CheA is active. The factor $\alpha \equiv k_A / (k_A + k_Z)$
410 is the fraction of CheY phosphorylated when all CheA are active, i.e. when the activity a = 1.
411 This model recapitulates the features of the data well. **Figure 5c** shows a fit to Eq. (7) (dotted
412 line) with parameters $\langle b \rangle$ = (6 ± 1) × 10^2 and α = 0.32 ± 0.02 (R^2 = 0.65; errors represent 95%
413 confidence interval). Analogous to "burst size" in stochastic gene expression[65,66], $\langle b \rangle$ increases
414 number fluctuations in CheY-P, which are intrinsically low due to the high CheY copy number (see
415 **SI Discussion**). The parameter α represents the fact that the contribution of CheA fluctuations
416 to CheY-P noise must go to zero (as in **Figure 5c**) when a = 1, which corresponds to a mean CW
417 bias of ~0.5. (We note that the noise suppression previously mentioned by Colin et al.[56] occurs in
418 the opposite limit of a = 0.) The value of α points to a kinetic ceiling on CheA-receptor complexes
419 of $k_A = 0.47k_Z$, or ~14 s^{-1} assuming a constant CheY-P dephosphorylation rate of k_Z = 30 s^{-1}, within
420 the reported range[54,60,61]. A maximum rate k_A = 14 s^{-1} is consistent with reported values of the
421 CheA auto-phosphorylation rate, the rate-limiting step for CheY phosphorylation[33,54,60,61]. (We
422 note that in the *ΔcheZ* strain, the kinetic ceiling on k_A would not cap [CheY-P] since k_Z = 0.)
423 Our observations suggest that network fluctuations are critical drivers for CW flagellar
424 rotation/tumbling in *E. coli*. Previous studies[36,42,67] proposed that waves of CheA activity could
425 cause transient increases in [CheY-P]. Our data and model appear to be consistent with this
426 mechanism, with the "burst size" $\langle b \rangle$ in Eq. (7) representing such waves in activity (see **Fig. 5d**
427 for a schematic depiction). Our fit parameters suggest that several hundred CheY molecules are
428 phosphorylated during such events, a not-insignificant fraction of the total number, estimated to
429 be ~8000[55]. We envision that transient increases in [CheY-P], driven by waves of phosphorylation
430 by the receptor kinase complex[36], increases the CW bias to generate tumbles. However, the
431 amount of cellular [CheY-P] is subject to the constraints of CheA phosphorylation kinetics. When
432 the cell experiences a network activating stimulus, and the receptor kinase complex is pushed to
433 its maximum activity, the cellular [CheY-P] reaches its upper limit. This is manifested as high CW
434 bias and suppressed fluctuations in CW bias.
435 Previous single-cell measurements of flagellar rotation by bead tracking[31,39] and of CheA
436 activity using fluorescent reporters[40,41] have reported long-term noise in the chemotaxis

437 network. This has largely been attributed to CheR-CheB methylation-demethylation
438 dynamics[31,68] and, recently, to new sources such as receptor clustering and other dynamics[40,41,67].
439 A direct comparison between these results and ours is difficult because of the differences in
440 timescales between the measurements (3-40 s vs. 10-1000 s). Notably, burst-like noise similar to
441 what we observe[36,42] has been attributed to cooperative receptor state switching[67]. While our
442 approach aligns with other recent work that extends noise measurements to fast timescales of
443 the order of run and tumble durations, photobleaching of the dyes limits the duration of our
444 traces and limits the overlap between the measurement timescales. For this reason, we have
445 deliberately made our model for CheA activity fluctuations in Eq. (7) agnostic to the source of
446 noise to allow for various possibilities. (We nevertheless note that the general form for CheA
447 activity noise is similar to that used by Colin et al.[56]; see **SI Discussion** for more details.)
448 The noise characteristics of the chemotaxis network revealed in our measurements may have
449 several functional consequences. First, network fluctuations may act to synchronize flagellar
450 switching[36,37,42,67], which was shown to make swimming behavior robust to variation in flagella
451 number[37]. *E. coli* has also been proposed to exploit long-timescale network fluctuations to
452 explore larger volumes of space[31,32] and to increase drift speeds, enhancing migration along
453 increasing attractant gradients[33–35]. In addition, our observation of a mean CW bias well below
454 the midpoint of the *c* vs CheY-P curve at steady state is consistent with theory and simulations[45]
455 predicting that cells' drift velocity along chemical gradients is maximized at low CW bias[47], an
456 idea supported by recent experiments[46]. Lastly, the kinetic ceiling in receptor kinase activity
457 which restricts network fluctuations when the mean [CheY-P] increases (as depicted in **Fig. 5d**)
458 may prevent CheY-P concentrations from saturating and leading to continuous and unproductive
459 CW flagellar rotation/tumbling. Such behavior could result in increased *E. coli* swimming
460 efficiency down steep decreases in attractant concentration, as likely found in natural
461 environments. These findings point to network fluctuations tuned to maximize chemotactic drift.
462

463 ## Acknowledgements

464 We are thankful to Tom Kuhlman for guiding us through the process of molecular cloning, and to
465 Howard Berg for providing bacterial strains. We thank members of the Chemla laboratory for

scientific discussions and Christopher Rao for providing comments on the manuscript. Work in the Chemla and Golding labs is supported by National Science Foundation Physics Frontiers Center (PFC) “Center for the Physics of Living Cells” (CPLC) PHY-1430124. Work in the Golding lab is supported by the National Institutes of Health grant no. R35 GM140709 and the Alfred P. Sloan Foundation.

Data availability

The datasets generated during and analyzed during the current study are available as an excel file included with this manuscript.

476 ## Materials and Methods

477 ### Microbiology

478 **Cell preparation**

479 Experiments were performed on the HCB1660 *E. coli* strain, a gift from the Berg lab[69]. This strain
480 is considered wild-type for chemotaxis but is *ΔfliC* expressing $FliC^{S219C}$ under the control of the
481 P_{araBAD} promoter. The mutant $FliC^{S219C}$ protein was specifically labelled with a cysteine reactive
482 fluorescent dye, Alexa Fluor 532 C_5 Maleimide (A10255, ThermoFisher Scientific) using the
483 method first described by Turner et al.[69] and later used by Mears et al.[37]. The strain referred to
484 as CheY* is PM87, *ΔfliC ΔcheBYZ* expressing $FliC^{S219C}$ and constitutively active $CheY^{D13K}$,
485 constructed by Mears et al.[37]. The strain referred to as RB03 (constructed for this work) is *ΔfliC*
486 *ΔcheZ* expressing $FliC^{S219C}$.

487 As described by Mears et al.[37], for each experiment, a single colony from an LB, lysogeny
488 broth, agar plate was inoculated into 1 mL tryptone broth (TB: 0.8% [wt/vol] NaCl, 1% Bacto
489 Tryptone), and grown to saturation overnight (14-18 hours), shaking at 265 RPM at 30°C with the
490 appropriate antibiotics. The overnight culture was diluted 100-fold into 12 mL TB, and grown to
491 OD_{600} ~0.4 to 0.5, with 0.01% [wt/vol] or 666 µM L-arabinose, shaking at 265 RPM at 30°C for
492 ~4.5 hours. The over-day culture was washed twice by slow centrifugation (1300 × *g*) and gently
493 resuspended in 1 mL motility buffer (MB: 10 mM Phosphate Buffer [pH 7.0], 70 mM NaCl and 0.1
494 mM EDTA)[21].

495 To label flagella fluorescently, we followed the protocol reported by Mears et al.[37]. An
496 appropriate volume of the Alexa Fluor 532 C_5 Maleimide dye was added to resuspended cells in
497 0.5 mL MB to a concentration of ~0.01 mg/mL and incubated with slow rotation (~10 RPM) at
498 room temperature in the dark for 90 min. The labeled cells were gently resuspended in 1 mL MB.
499 For trapping, cells were diluted 20-fold in trap motility buffer (TMB: 70 mM NaCl, 100 mM Tris-
500 Cl, 2% [wt/vol] glucose, with 0.1 mM methionine and an oxygen-scavenging system [290 µg ml^{-1}
501 pyranose oxidase and 65 µg ml^{-1} catalase][38]) and injected into the flow chamber for the trapping
502 experiment. When handling resuspended cells, at all times, we avoided pipetting, or we used
503 wide orifice pipette tips to avoid shearing flagella.

504 1 mg of the dry Alexa Fluor 532 C_5 Maleimide dye was dissolved in 250 µL water by vortexing
505 and stored in aliquots at -20°C. The stock concentration for each aliquot was determined using
506 UV-Visible Absorption Spectroscopy. Since this dye does not dissolve readily in water, we found
507 it important to determine the concentration for each aliquot separately for optimal labeling.
508

509 **Construction of strains**

510 The bacterial strains and plasmids used for this work are listed in **Table 1**. Oligonucleotides for
511 generating mutations and creating plasmids are listed in **Table 2.** All primers were purchased
512 from Integrated DNA Technologies (Coralville, Iowa). The *CheZ* chromosomal deletion was carried
513 out using the standard λ Red recombinase system developed by Datsenko and Wanner[70]. The
514 strain referred to as RB03 was created from HCB1613 (AW405, chemotaxis wild-type with a
515 functional FliC deletion). To create the strain RB01, *CheZ* was replaced by a chloramphenicol
516 resistance cassette with flanking FRT (Flp recombinase-recombination target) sites using the
517 primers CheZ-pKDF and CheZ-pKDR with pKD3 as a template. This replacement was accomplished
518 via the λ Red recombinase enzymes expressed from pKD46. The chloramphenicol cassette was
519 eliminated via Flp recombinase expressed from pCP20 to obtain strain RB02. Finally, the strain
520 RB03 was created by transforming strain RB02 with the plasmid pBAD33 that expresses $FliC^{S219C}$.
521 Standard molecular cloning techniques were used to purify plasmids and perform PCRs.
522

523 ## Data Acquisition

524 **Optical trapping of individual *E. coli* with simultaneous fluorescence imaging**

525 Experiments were performed with a dual-trap optical tweezers instrument combined with epi-
526 fluorescence slim-field imaging, developed and described in detail in previous work by Mears et
527 al.[37]. Briefly, the optical traps were created from a single 5-W, 1064-nm laser (YLR-5-1064-LP, IPG
528 Photonics). Two trapping beams were generated by timesharing, intermittently deflecting the
529 input beam between two positions with an Acousto-Optic Deflector, AOD (DTSXY-250-1064, AA
530 Opto-Electronic). The two resulting beams were then tightly focused using a 60X, water
531 immersion (1.2 NA) objective (Nikon, Tokyo, Japan) to create two optical traps. An identical
532 objective was used to collect the transmitted trap light for position detection and for bright-field

533 imaging of the cells using Koehler illumination from a blue LED. A bacterial cell could be captured
534 and aligned between the two optical traps without impeding its rotatory motion. The light
535 scattered by the trapped cell was collected onto a position sensitive photodetector and used to
536 monitor cell motion, which was analyzed to determine runs and tumbles as described below and
537 previously by Min et al.[38].

538 Fluorescently labeled flagella of trapped cells were imaged using a 532-nm laser (TECGL-30,
539 World Star Tech) aligned for slim-field illumination[71], with the excitation beam diameter at the
540 sample plane ~10-15 µm. We strobed the fluorescence excitation and trap laser illumination out
541 of phase with each other to minimize photobleaching[37]. The fluorescence illumination was
542 strobed by using an Acousto-Optic Modulator, AOM (802AF1, IntraAction) to deflect the
543 excitation light intermittently into the sample plane for a duration of 16-20 µs each cycle while
544 the traps were off. An EMCCD camera (iXon3 860 EMCCD, Andor) recorded images in synchrony
545 with the excitation pulse at the rate of 100 frames per second to capture focused images of the
546 flagella as they rotated at a rate of ~100 Hz. In this manner, movies of flagellar motion were
547 recorded, and flagella waveforms were analyzed until the flagella photobleached, typically for
548 10-20 for unstimulated cells and 20-40 s for stimulated cells. Movies were saved using the Solis
549 software (Andor) and processed using custom written code in MATLAB. Each movie was analyzed
550 manually to count flagella and their transitions between CW and CCW rotating states.

551

552 **Motility assays combined with fluorescence imaging in trapped cells**

553 Custom-built microfluidic chambers shown in **Figure 1c** and **4a** (preparation described in detail
554 in Mears et al.[37] and Min et al.[43]) were used to perform motility assays coupled with fluorescence
555 imaging of labeled flagella on individual trapped cells. To prepare chambers, glass coverslips were
556 sonicated in acetone, then rinsed in deionized water. This step was followed by rinsing in
557 methanol and drying under nitrogen flow. The flow channels in the chamber were cut out from
558 Nescofilm (Alfresa Pharma Corporation, Osaka, Japan) and bonded to glass coverslips as
559 described previously[37,43].

560 For measurements of free-swimming, or unstimulated, cells, the chamber contained two
561 channels (**Figure 1c**). The upper channel contained trap motility buffer (TMB) only, while the

562 lower channel contained *E. coli* cells in TMB. Both channels were continuously injected with the
563 appropriate solutions using a syringe pump (PHD2000, Harvard Apparatus) with a linear flow rate
564 of ~30 µm/s. Cells were trapped in the lower channel and moved to the upper channel by
565 displacing the chamber with respect to the traps using a motorized three-axis translational stage
566 (ESP301; Newport, Irvine, California). Once the trapped cell was aligned between the two traps
567 in the upper channel, the bright-field illumination was turned off and the 532-nm excitation
568 illumination was turned on. Cell motion was observed by simultaneously recording the optical
569 trap signal sensed by position sensitive photodetectors and the fluorescence signal from labelled
570 flagella sensed by the EMCCD camera.

571 For measurements of stimulated cells undergoing chemotactic adaptation, the chamber
572 contained three channels (**Figure 4a**). For a step-down stimulus, the top ("blank") channel
573 contained TMB only, the middle ("blank + attractant") channel contained TMB, 1 mM α-methyl-
574 DL-aspartate (MeAsp) and Rhodamine B (100 nM), and the bottom ("cell + attractant") channel
575 contained TMB, 1 mM MeAsp and *E. coli* cells. Fluorescence imaging of the Rhodamine B diffusion
576 profile was used to characterize the gradient formed across the top and the middle channel, as
577 described by Min et al.[43]. All three channels of the flow chamber were injected with their
578 solutions at a linear flow rate of ~50 µm/s. In a typical experiment, a swimming cell was first
579 captured from the "cells + attractant" channel. The trapped cell was moved to the "blank +
580 attractant" channel, aligned between the two traps, and oriented along the direction of the flow.
581 Pre-stimulus optical trap signal of the swimming cell was recorded for ~200 s (without any
582 fluorescence imaging of flagella). The trapped cell was then moved at the speed 100 µm/s to the
583 "blank" channel so that it experienced a step down in MeAsp concentration. While the entire
584 move took 10 s, the interface between channels where the step down occurred was crossed in
585 ~4 s (where the interface is defined as the distance from 10% to 90% of the chemoattractant
586 concentration, as shown in Figure S1 in Min et al.[43]). t = 0 was defined as the end of this move.
587 During the move, the bright field illumination was turned off and the 532-nm excitation
588 illumination was turned on. The chemotactic response of the captured cell was recorded in the
589 "blank" channel by simultaneously recording the optical trap signal and the fluorescence signal

590 from labelled flagella. While the trap signal post-stimulus was recorded for ~400 s, the EMCCD
591 signal was recorded only for ~30-40 s until the flagella photobleached.
592

593 ## Raw Data Analysis

594 **Run-tumble analysis for optical trap data**

595 Cell motion was detected from imaging the optical trap light scattered by the cell body onto
596 position-sensitive photodetectors, as described previously by Min et al.[38]. This optical trap signal
597 was analyzed for runs and tumbles. Briefly, runs corresponded to oscillatory signals due to cell
598 body roll at a frequency ~10 Hz, while tumbles corresponded to erratic trap signals with a
599 frequency <1 Hz. We used custom-written MATLAB code incorporating a wavelet analysis to
600 identify the peak body roll frequency at every time point of each data trace and to assign runs
601 and tumbles by specifying an appropriate frequency threshold[38]. An example trace of the trap
602 signal and the corresponding run-tumble assignment is shown in **Figure 1c** and **d** in earlier work
603 by Mears et al.[37].
604

605 **Image analysis for fluorescence data**

606 Images acquired using the high-speed fluorescence imaging described above were adjusted for
607 contrast to best visualize the flagella. Each movie was played in slow motion and Clockwise
608 (CW)/Counter Clockwise (CCW) states were assigned manually to each flagellum over a time
609 window of 100 ms (i.e. 10 frames). As described previously[21,37], the CCW/CW rotation state of
610 the flagella can be visually identified from their different helical waveforms, commonly referred
611 to as 'normal', 'semi-coiled', 'curly-1' and 'curly-2'. CCW-rotating flagella exclusively adopt the
612 'normal' waveform and CW-rotating flagella adopt the 'semi-coiled' and 'curly-1' waveforms the
613 majority of the time. Waveform transitions take less than ~0.5 s to propagate through the
614 flagella.
615

616 ## Modeling and Analysis

617 **Extracting CW bias fluctuations from flagellar rotation data**

In flagellar imaging movies of individual cells, we tracked the CW/CCW state of each flagellum—hence the number of CW flagella in time—and determined $p_N(n_{cw})$, the probability that n_{cw} out of a total of N flagella rotate CW, where $n_{cw} = 0, 1\ldots N$. From first principles[72], we can relate $p_N(n_{cw})$ to the instantaneous CW bias of the motor, c, the probability that a motor rotates CW, through Eq. (1), where $p(c)$ is the distribution in motor bias c. $p_N(n_{cw}\,|\,c)$, the conditional probability that n_{cw} out of N flagella are CW given a certain bias c, is given by the binomial distribution in Eq. (2), since as shown in previous work by Mears et al.[37], the flagellar motors switch independently.

We can thus use Eq. (1) and (2) to extract information on the motor bias distribution $p(c)$ from measurements of $p_N(n_{cw})$. In general, this integral equation cannot be solved by a unique solution $p(c)$. Instead, a finite number of moments of $p(c)$ can be determined, which increases as the number of flagella N increases. Using Eq. (1) and (2), one can relate moments of $p_N(n_{cw})$ to those of $p(c)$. For the first two moments, it can be shown that:

$$\begin{aligned}\langle n_{cw}\rangle &= \sum_{n_{cw}=0}^{N} n_{cw} p_N(n_{cw}) = \int_0^1 dc \sum_{n_{cw}=0}^{N} n_{cw} \binom{N}{n_{cw}} c^{n_{cw}} (1-c)^{N-n_{cw}} p(c) \\ &= \int_0^1 dc\, Ncp(c) = N\langle c\rangle,\end{aligned} \tag{8}$$

and

$$\begin{aligned}\langle n_{cw}(n_{cw}-1)\rangle &= \sum_{n_{cw}=0}^{N} n_{cw}(n_{cw}-1) p_N(n_{cw}) = \int_0^1 dc \sum_{n_{cw}=0}^{N} n_{cw}(n_{cw}-1) \binom{N}{n_{cw}} c^{n_{cw}} (1-c)^{N-n_{cw}} p(c) \\ &= \int_0^1 dc\, N(N-1)c^2 p(c) = N(N-1)\langle c^2\rangle.\end{aligned} \tag{9}$$

Eqs. (8) and (9) can be manipulated to give Eqs. (3) and (4) for the mean and variance of the CW bias in the text. We note that Eq. (9) shows that $\langle c^2\rangle$ can be determined only from cells with $N \geq 2$ flagella. The first two moments are generally adequate for our purposes to assess fluctuations in the network, and we analyzed cells with $N \geq 2$. In principle, this approach can be extended to determine higher moments (of order $n \geq 3$), which reveal finer features of the CW bias distribution $p(c)$ (e.g. skew, kurtosis, etc.). We chose not to determine these higher moments due to the limited amount of cells with $N \geq n$ flagella.

640 Since the form of the distribution $p_N(n_{cw})$ depends on the number of flagella, we analyzed
641 cells with different numbers of flagella *N* separately, as shown in **Figure 2a** and **d**. For each
642 population of cells, we determined the mean and standard deviation in CW bias and estimated
643 their errors by bootstrapping, where individual cell time traces were resampled with replacement
644 to generate different $p_N(n_{cw})$ for each bootstrap trial. We also determined global values for these
645 parameters across the population of cells with different *N* by carrying out an inverse-variance
646 weighted average over their values for each *N*. The errors were determined using the customary
647 expression for the standard error of a weighted mean.

648 Finally, we also used distributions $p_N(n_{cw})$ obtained from each individual cell to determine
649 the mean and standard deviation in CW bias from each cell (**Figure 3**). The errors in these
650 parameters were estimated using bootstrapping. Here, 0.5-s long time windows of individual cell
651 time traces of n_{cw} were resampled with replacement to construct traces and corresponding
652 $p_N(n_{cw})$ for each bootstrapping trial. A 0.5-s window duration was chosen based on the average
653 autocorrelation time for individual cell n_{cw} time traces, determined to be ~0.3 s across *N* (data
654 not shown). Time windows of duration of 0.5 s, about twice as long as the autocorrelation time,
655 are sufficiently long to be uncorrelated and suitable for the purposes of bootstrapping.
656

657 **Variance decomposition**

658 The variance in CW bias measured over a population of cells contains contributions from the
659 single-cell CW bias variance and from cell-cell differences in mean CW bias. We decomposed the
660 variance over the population (the set {cell}) to determine the intra- and inter-cell contributions,
661 using the Law of Total Variance[73]:

662 $$\mathrm{var}(c\,|\,\{\mathrm{cell}\}) = \mathrm{E}[\mathrm{var}(c\,|\,\mathrm{cell})] + \mathrm{var}(\mathrm{E}[c\,|\,\mathrm{cell}]), \quad (10)$$

663 where E[…] is the expectation value and var is the variance. Based on established interpretations
664 of Eq. (10), the first term on the right-hand side represents the contribution of the average single-
665 cell variance in CW bias, which is determined from the mean of the individual variances in CW
666 bias for each cell for a given *N.* The second term on the right hand side is the contribution of the

667 cell-to-cell variation in CW bias, which is determined from the variance in the mean CW bias for
668 each cell for a given a *N*.
669
670 **Estimating CW bias fluctuations for stimulated cells**
671 The flagellar imaging data for trapped cells experiencing a step-down in MeAsp were also
672 analyzed to record the number of CW flagella with time. Since the motor bias varies with time
673 during adaptation, each individual cell time trace was divided into non-overlapping windows the
674 duration of which was determined from the cell's adaptation time. For each cell, the collected
675 optical trap signal was analyzed for runs and tumbles, and the tumble bias was calculated from
676 the fraction of time the cell tumbled over a 10-s sliding time window. The time trace of the tumble
677 bias was fit to the following expression:

678 $$TB(t) = TB_{\infty} + ae^{-bt} + ce^{-dt} \quad (11)$$

679 where *a, b, c* and *d* are fitting parameters, and TB_{∞} is the tumble bias of the cell when it has
680 adapted to the stimulus. The adaptation time was approximated as $t_{adap} = \ln(2)/b$ following a
681 procedure used by Min et al.[43] An example fit to Eq. (11) is shown in **Supplementary Figure S1.**
682 Windows of duration $0.2t_{adap}$ were selected starting at the time when the trapped cell was
683 moved to the top channel, $t = 0$, until $t = 1.6t_{adap}$, where t_{adap} for our dataset was found to be ~13
684 s. A final window of variable length between $0.5t_{adap}$ and $2.5t_{adap}$ was created based on the
685 number of data points left in the trace. Data for number of CW flagella n_{cw} from multiple cells
686 with the same total number of flagella *N* were pooled in each time window. The time-dependent
687 histogram $p_N(n_{cw}, t)$ was constructed and the time-dependent mean and standard deviation in
688 CW bias was determined for each time window. The $0.2t_{adap}$ time windows, corresponding to a
689 2.6-s duration on average, were sufficiently short so that the average tumble bias was constant
690 to within ~10-20%, but long enough to enable a reliable estimate of the mean and CV in CW bias
691 given the data set size. The error was calculated by bootstrap resampling as before, over each
692 time window. We calculated the mean and standard deviation in CW bias globally across all *N* for
693 each time window as described previously.

694 **Table 1**

695 Strains and Plasmids used in this study

Strain	Genotype	Comments	Source
HCB1613	*fliC*::Tn5 (Kan^R)	wild type "deleted" for fliC	Gift of Berg lab
HCB1660	*fliC*::Tn5 (Kan^R)	wild type "deleted" for fliC expressing pBAD33- $fliC^{S219C}$	Gift of Berg lab
RB01	*cheZ*::Cm, *fliC*::Tn5 (Kan^R)	N/A	This work
RB02	*cheZ*::FRT, *fliC*::Tn5 (Kan^R)	N/A	This work
RB03	*cheZ*::FRT, *fliC*::Tn5 (Kan^R)	wild type "deleted" for fliC and cheZ expressing pBAD33- $fliC^{S219C}$	This work
Plasmids			
pKD3		Template for Cm^R cassette	[70]
pKD46		Plasmid expressing λ Red recombinases	[70]
pCP20		Plasmid expressing Flp recombinase	[70]
pBAD33	*$fliC^{S219C}$* under P_{araBAD} promoter, Cm^R, p15a origin	Expresses mutant version of FliC for fluorescence labelling	[69]gift of Berg lab

696

697 **Table 2**

698 Primers used in this work

Primer	Sequence
CheZ-pKDF	GGAAAAACTCAACAAAATCTTTGAGAAACTGGGCATGTGAG

	GATGCGACTGTGTAGGCTGGAGCTGCTTC
CheZ-pKDR	TTATCAGACCGCCTGATATGACGTGGTCACGCCACATCAGGC AATACAAACATATGAATATCCTCCTTA

Table 3

CW bias parameters for the wild type strain

N	Mean CW bias, μ_c	Standard deviation in CW bias, σ_c	Coefficient of Variation, σ_c/μ_c
2	0.18 ± 0.03	0.25 ± 0.02	1.4 ± 0.3
3	0.14 ± 0.03	0.22 ± 0.02	1.6 ± 0.4
4	0.07 ± 0.02	0.14 ± 0.02	2.0 ± 0.6
5	0.17 ± 0.05	0.22 ± 0.03	1.3 ± 0.4
Global	0.12 ± 0.01	0.20 ± 0.01	1.5 ± 0.2

Table 4

CW bias parameters for the mutant CheY* strain

N	Mean CW bias, μ_c	Standard deviation in CW bias, σ_c	Coefficient of Variation, σ_c/μ_c
2	0.31 ± 0.09	0.29 ± 0.06	1.0 ± 0.3
3	0.26 ± 0.05	0.17 ± 0.03	0.6 ± 0.2
4	0.19 ± 0.03	0.14 ± 0.03	0.7 ± 0.2
5	0.11 ± 0.04	0.13 ± 0.03	1.2 ± 0.5
Global	0.19 ± 0.02	0.16 ± 0.02	0.7 ± 0.1

706 ## References

707 1. Lim WA, Mayer B., P. T. *Cell Signaling*. (Garland Science, 2014).

708 2. Mcadams, H. H. & Arkin, A. Stochastic mechanisms in gene expression. *Proc. Natl. Acad.*
709 *Sci. U. S. A.* **94**, 814–819 (1997).

710 3. Allen, C. & Stevens, C. F. An evaluation of causes for unreliability of synaptic
711 transmission. *Proc. Natl. Acad. Sci. U. S. A.* **91**, 10380–10383 (1994).

712 4. Barkai, N. & Leibler, S. Robustness in simple biochemical networks to transfer and
713 process information. *Nature* **387**, 913–917 (1997).

714 5. Silva-Rocha, R. & de Lorenzo, V. Noise and Robustness in Prokaryotic Regulatory
715 Networks. *Annu. Rev. Microbiol.* **64**, 257–275 (2010).

716 6. Stelling, J., Sauer, U., Szallasi, Z., Doyle, F. J. & Doyle, J. Robustness of Cellular Functions.
717 *Cell* **118**, 675–685 (2004).

718 7. Eldar, A. *et al.* Robustness of the BMP morphogen gradient in Drosophila embryonic
719 patterning. *Nature* **419**, 304–308 (2002).

720 8. Rao, C. V, Wolf, D. M. & Arkin, A. P. Control, exploitation and tolerance of intracellular
721 noise. *Nature* **420**, 231–237 (2002).

722 9. Tsimring, L. S. Noise in biology. *Reports Prog. Phys.* **77**, (2014).

723 10. Raj, A. & van Oudenaarden, A. Nature, nurture, or chance: stochastic gene expression
724 and its consequences. *Cell* **135**, 216–26 (2008).

725 11. Eldar, A. & Elowitz, M. B. Functional roles for noise in genetic circuits. *Nature* **467**, 167–
726 173 (2010).

727 12. Balázsi, G., Van Oudenaarden, A. & Collins, J. J. Cellular decision making and biological
728 noise: From microbes to mammals. *Cell* **144**, 910–925 (2011).

729 13. Wadhams, G. H. & Armitage, J. P. Making sense of it all: bacterial chemotaxis.

730 *Nat.Rev.Mol.Cell Biol.* **5**, 1024–1037 (2004).

731 14. Shimizu, T. S., Tu, Y. & Berg, H. C. A modular gradient-sensing network for chemotaxis in
732 Escherichia coli revealed by responses to time-varying stimuli. *Mol. Syst. Biol.* **6**, 1–14
733 (2010).

734 15. Lan, G., Schulmeister, S., Sourjik, V. & Tu, Y. Adapt locally and act globally: Strategy to
735 maintain high chemoreceptor sensitivity in complex environments. *Mol. Syst. Biol.* **7**, 1–
736 16 (2011).

737 16. Sourjik, V. & Wingreen, N. S. Responding to chemical gradients: bacterial chemotaxis.
738 *Curr. Opin. Cell Biol.* **24**, 262–8 (2012).

739 17. Micali, G. & Endres, R. G. Bacterial chemotaxis: Information processing, thermodynamics,
740 and behavior. *Curr. Opin. Microbiol.* **30**, 8–15 (2016).

741 18. Larsen, S. H., Reader, R. W., Kort, E. N., Tso, W. W. & Adler, J. Change in direction of
742 flagellar rotation is the basis of the chemotactic response in Escherichia coli. *Nature* **249**,
743 74–77 (1974).

744 19. Macnab, R. M. & Ornston, M. K. Normal-to-curly flagellar transitions and their role in
745 bacterial tumbling. Stabilization of an alternative quaternary structure by mechanical
746 force. *J. Mol. Biol.* **112**, 1–30 (1977).

747 20. Turner, L., Ryu, W. S. & Berg, H. C. Real-time imaging of fluorescent flagellar filaments. *J.*
748 *Bacteriol.* **182**, 2793–2801 (2000).

749 21. Darnton, N. C., Turner, L., Rojevsky, S. & Berg, H. C. On torque and tumbling in swimming
750 Escherichia coli. *J. Bacteriol.* **189**, 1756–1764 (2007).

751 22. Parkinson, J. S., Hazelbauer, G. L. & Falke, J. J. Signaling and sensory adaptation in
752 Escherichia coli chemoreceptors: 2015 update. *Trends Microbiol.* **23**, 257–266 (2015).

753 23. Scharf, B. E., Fahrner, K. A., Turner, L. & Berg, H. C. Control of direction of flagellar
754 rotation in bacterial chemotaxis. *Proc. Natl. Acad. Sci.* **95**, 201–206 (1998).

755 24. Alon, U. *et al.* Response regulator output in bacterial chemotaxis. *EMBO J.* **17**, 4238–4248
756 (1998).

757 25. Cluzel, P., Surette, M. & Leibler, S. An Ultrasensitive Bacterial Motor Revealed by
758 Monitoring Signaling Proteins in Single Cells. *Science (80-.).* **287**, 1652–1655 (2000).

759 26. Hess, J. F., Oosawa, K., Kaplan, N. & Simon, M. I. Phosphorylation of three proteins in the
760 signaling pathway of bacterial chemotaxis. *Cell* **53**, 79–87 (1988).

761 27. Blat, Y. & Eisenbach, M. Phosphorylation-Dependent Binding of the Chemotaxis Signal
762 Molecule CheY to Its Phosphatase, CheZ. *Biochemistry* **33**, 902–906 (1994).

763 28. Springer, M. S., Goy, M. F. & Adler, J. Protein methylation in behavioural control
764 mechanisms and in signal transduction. *Nature* **280**, 279–284 (1979).

765 29. Kehry, M. R., Bond, M. W., Hunkapiller, M. W. & Dahlquist, F. W. Enzymatic deamidation
766 of methyl-accepting chemotaxis proteins in Escherichia coli catalyzed by the cheB gene
767 product. *Proc. Natl. Acad. Sci. U. S. A.* **80**, 3599–3603 (1983).

768 30. Borkovich, K. A., Alex, L. A. & Simon, M. I. Attenuation of sensory receptor signaling by
769 covalent modification. *Proc. Natl. Acad. Sci.* **89**, 6756–6760 (1992).

770 31. Korobkova, E., Emonet, T., Vilar, J. M. G., Shimizu, T. S. & Cluzel, P. From molecular noise
771 to behavioural variability in a single bacterium. *Nature* **428**, 574–578 (2004).

772 32. Matthäus, F., Jagodič, M. & Dobnikar, J. E. coli superdiffusion and chemotaxis-search
773 strategy, precision, and motility. *Biophys. J.* **97**, 946–957 (2009).

774 33. Emonet, T. & Cluzel, P. Relationship between cellular response and behavioral variability
775 in bacterial chemotaxis. *Proc. Natl. Acad. Sci. U. S. A.* **105**, 3304–3309 (2008).

776 34. He, R., Zhang, R. & Yuan, J. Noise-Induced Increase of Sensitivity in Bacterial Chemotaxis.
777 *Biophys. J.* **111**, 430–437 (2016).

778 35. Flores, M., Shimizu, T. S., ten Wolde, P. R. & Tostevin, F. Signaling Noise Enhances
779 Chemotactic Drift of E. coli. *Phys. Rev. Lett.* **109**, 148101 (2012).

780 36. Terasawa, S. *et al.* Coordinated reversal of flagellar motors on a single Escherichia coli
781 cell. *Biophys. J.* **100**, 2193–2200 (2011).

782 37. Mears, P. J., Koirala, S., Rao, C. V., Golding, I. & Chemla, Y. R. Escherichia coli swimming is
783 robust against variations in flagellar number. *Elife* **3**, 1–18 (2014).

784 38. Min, T. L. *et al.* High-resolution, long-term characterization of bacterial motility using
785 optical tweezers. *Nat. Methods* **6**, 831–835 (2009).

786 39. Park, H. *et al.* Interdependence of behavioural variability and response to small stimuli in
787 bacteria. *Nature* **468**, 819–821 (2010).

788 40. Keegstra, J. M. *et al.* Phenotypic diversity and temporal variability in a bacterial signaling
789 network revealed by single-cell FRET. *Elife* **6**, 1–33 (2017).

790 41. Colin, R., Rosazza, C., Vaknin, A. & Sourjik, V. Multiple sources of slow activity
791 fluctuations in a bacterial chemosensory network. *Elife* **6**, 1–32 (2017).

792 42. Che, Y. S. *et al.* Fluctuations in intracellular chey-p concentration coordinate reversals of
793 flagellar motors in E. Coli. *Biomolecules* **10**, 1–20 (2020).

794 43. Min, T. L., Mears, P. J., Golding, I. & Chemla, Y. R. Chemotactic adaptation kinetics of
795 individual Escherichia coli cells. *Proc. Natl. Acad. Sci.* **109**, 9869–9874 (2012).

796 44. Shamir, M., Bar-On, Y., Phillips, R. & Milo, R. SnapShot: Timescales in Cell Biology. *Cell*
797 **164**, 1302-1302.e1 (2016).

798 45. Dufour, Y. S., Fu, X., Hernandez-Nunez, L. & Emonet, T. Limits of Feedback Control in
799 Bacterial Chemotaxis. *PLoS Comput. Biol.* **10**, e1003694 (2014).

800 46. Wong-Ng, J., Melbinger, A., Celani, A. & Vergassola, M. The Role of Adaptation in
801 Bacterial Speed Races. *PLoS Comput. Biol.* **12**, 1–15 (2016).

802 47. Waite, A. J., Frankel, N. W. & Emonet, T. Behavioral Variability and Phenotypic Diversity
803 in Bacterial Chemotaxis. *Annu. Rev. Biophys.* **47**, 595–616 (2018).

804 48. Alon, U., Surette, M. G., Barkai, N. & Leibler, S. Robustness in bacterial chemotaxis.

805 *Nature* **397**, 168–171 (1999).

806 49. Sourjik, V. & Berg, H. C. Receptor sensitivity in bacterial chemotaxis. *Proc. Natl. Acad. Sci.*
807 *U. S. A.* **99**, 123–127 (2002).

808 50. Segall, J. E., Block, S. M. & Berg, H. C. Temporal comparisons in bacterial chemotaxis.
809 *Proc. Natl. Acad. Sci. U. S. A.* **83**, 8987–8991 (1986).

810 51. Block, S. M., Segall, J. E. & Berg, H. C. Adaptation kinetics in bacterial chemotaxis. *J.*
811 *Bacteriol.* **154**, 312–323 (1983).

812 52. Mesibov, R. & Adler, J. Chemotaxis toward amino-acids in Escherichia coli. *J. Bacteriol.*
813 **112**, 315–326 (1972).

814 53. Mesibov, R., Ordal, G. W. & Adler, J. The range of attractant concentrations for bacterial
815 chemotaxis and the threshold and size of response over this range. Weber law and
816 related phenomena. *J. Gen. Physiol.* **62**, 203–223 (1973).

817 54. Vladimirov, N., Løvdok, L., Lebiedz, D. & Sourjik, V. Dependence of bacterial chemotaxis
818 on gradient shape and adaptation rate. *PLoS Comput. Biol.* **4**, (2008).

819 55. Li, M. & Hazelbauer, G. L. Cellular stoichiometries of the components of the chemotaxis
820 signaling complex. *J. Bacteriol* **186**, 3687–3694 (2004).

821 56. Colin, R., Rosazza, C., Vaknin, A. & Sourjik, V. Multiple sources of slow activity
822 fluctuations in a bacterial chemosensory network. doi:10.7554/eLife.26796

823 57. Paulsson, J. Summing up the noise in gene networks. *Nature* **427**, 415–8 (2004).

824 58. Yue, G., Zhang, R. & Yuan, J. Timescale separation in the coordinated switching of
825 bacterial flagellar motors. *Phys. Biol.* **20**, (2023).

826 59. Yuan, J. & Berg, H. C. Ultrasensitivity of an adaptive bacterial motor. *J. Mol. Biol.* **425**,
827 1760–1764 (2013).

828 60. Bitbol, A. F. & Wingreen, N. S. Fundamental constraints on the abundances of chemotaxis
829 proteins. *Biophys. J.* **108**, 1293–1305 (2015).

830 61. Clausznitzer, D., Oleksiuk, O., Løvdok, L., Sourjik, V. & Endres, R. G. Chemotactic response
831 and adaptation dynamics in Escherichia coli. *PLoS Comput. Biol.* **6**, 1–11 (2010).

832 62. Lele, P. P., Shrivastava, A., Roland, T. & Berg, H. C. Response thresholds in bacterial
833 chemotaxis. *Sci. Adv.* **1**, e1500299 (2015).

834 63. Paulsson, J. Models of stochastic gene expression. *Phys. Life Rev.* **2**, 157–175 (2005).

835 64. Sourjik, V. & Berg, H. C. Binding of the Escherichia coli response regulator CheY to its
836 target measured in vivo by fluorescence resonance energy transfer. *Proc. Natl. Acad. Sci.*
837 *U. S. A.* **99**, 12669–12674 (2002).

838 65. Golding, I., Paulsson, J., Zawilski, S. M. & Cox, E. C. Real-time kinetics of gene activity in
839 individual bacteria. *Cell* **123**, 1025–1036 (2005).

840 66. Thattai, M. & van Oudenaarden, A. Intrinsic noise in gene regulatory networks. *Proc.*
841 *Natl. Acad. Sci.* **98**, 8614–8619 (2001).

842 67. Namba, T. & Shibata, T. Propagation of regulatory fluctuations induces coordinated
843 switching of flagellar motors in chemotaxis signaling pathway of single bacteria. *J. Theor.*
844 *Biol.* **454**, 367–375 (2018).

845 68. Roy, U. & Gopalakrishnan, M. Ultrasensitivity and fluctuations in the Barkai-Leibler model
846 of chemotaxis receptors in Escherichia coli. *PLoS One* **12**, 1–29 (2017).

847 69. Turner, L., Zhang, R., Darnton, N. C. & Berg, H. C. Visualization of flagella during bacterial
848 swarming. *J. Bacteriol.* **192**, 3259–3267 (2010).

849 70. Datsenko, K. A. One-step inactivation of chromosomal genes in Escherichia coli K-12
850 using PCR products. *Proc. Natl. Acad. Sci.* **97**, 6640–6645 (2000).

851 71. Plank, M., Wadhams, G. H. & Leake, M. C. Millisecond timescale slimfield imaging and
852 automated quantification of single fluorescent protein molecules for use in probing
853 complex biological processes. *Integr. Biol. (Camb).* **1**, 602–612 (2009).

854 72. Ross, S. M. *A first course in probability*. (Pearson, 2013).

73. Weiss, N. A. *A Course in Probability*. (Addison–Wesley, 2005).